Results in Materials 28 (2025) 100774

Contents lists available at ScienceDirect

Results in Materials

journal homepage: www.sciencedirect.com/journal/results-in-materials

Thermodynamic and kinetic analyses of high temperature oxidation of 316L stainless steel

Mohammad Maroufkhani [a], Alireza Khodabandeh [a], Iulian Radu [b], Elmira Moosavi-Khoonsari [a], Mohammad Jahazi [a,*]

[a] Department of Mechanical Engineering, École de Technologie Supérieure (ÉTS), Montreal, Quebec, Canada
[b] PCL Construction Company, Edmonton, Alberta, Canada

ARTICLE INFO

Keywords:
316L stainless steel
Activation energy
Isoconversional methods
Kinetics
Reaction mechanism
Solid state oxidation
Thermodynamics

ABSTRACT

This study investigates the thermodynamic behavior and non-isothermal oxidation kinetics of 316L stainless steel in the temperature range of 1100 K–1373 K, with relevance to the heat-affected zone during welding in oil and gas pipeline applications. Thermogravimetric analysis was performed at heating rates of 5, 10, 15, 20, and 25 K/min study the high-temperature oxidation kinetics of AISI 316L stainless steel welds. Kinetic analysis was conducted using Kennedy-Clark and Coats-Redfern methods as well as Friedman, Starink, Kissinger-Akahira-Sunose, and Flynn-Wall-Ozawa model-free isoconversional methods. Activation energies determined using isoconversional models ranged from 224.79 to 233.81 kJ/mol. The second-order (F2) and third-order (F3) reaction models provided the best fit to the experimental data, as confirmed by Criado master plot analysis. Thermodynamic properties ($\Delta H^{\neq}$., $\Delta S^{\neq}$., $\Delta G^{\neq}$) were also calculated for isocoversional models. FactSage thermochemical simulations revealed the formation of a dual-layer protective oxide scale primarily composed of spinel and corundum phases. These oxide layers enhance oxidation resistance at high temperatures. The findings contribute to a mechanistic and kinetic understanding of high-temperature oxidation in 316L stainless steel, supporting its reliable application in demanding oil and gas environments.

Nomenclature

TGA	Thermogravimetric analysis	CR	Coats-Redfern
Kp	Parabolic rate constant	t	Time (s)
E_a	Activation energy (kJ/mol)	A	Pre-exponential factor
DTA	Differential Thermal Analysis	MFR	Modified Friedman
FWO	Flynn-Wall-Ozawa	R	Gas constant 8.314 (J/mol·K)
T_p	Peak temperature (K)	KAS	Kissinger-Akahira-Sunose
α	Degree of conversion	*Wt*	Weight percentage (%)
KC	Kennedy-Clark	DTG	Differential thermogravimetric
β	Heating rate (K/min)	T	Temperature (K)
$g(\alpha)$	Integral form of the reaction model	R^2	Correlation coefficient
$\Delta H^{\neq}$	Enthalpy of activation	$\Delta S^{\neq}$	Entropy of activation
$\Delta G^{\neq}$	Gibbs energy of activation	*h*	Planck's constant (6.626×10^{-34} J s)
k_B	Boltzmann's constant (1.381×10^{-23} J/K)		

1. Introduction

316L stainless steel belongs to the austenitic alloy family and is widely recognized for its superior resistance to corrosion as well as its robust mechanical properties. [1]. Stainless steels, particularly 316L, are widely utilized in industries such as chemical processing, pipeline, and aerospace due to their ability to form a protective oxide layer that impedes further oxidation and corrosion [1,2]. The protective nature of oxide layer is primarily attributed to the formation of Cr_2O_3, which acts as a barrier to oxygen diffusion and helps in improving their resistance to corrosion. [3]. However, the stability of this protective layer can be compromised under certain service conditions, particularly during welding processes. In welding applications, especially on the root side of the weld, the presence of residual oxygen in the backing gas (ranging from 50 to 5000 ppm) can lead to high-temperature oxidation and discoloration [4]. This discoloration is not merely aesthetic; it indicates a change in surface chemistry and oxide structure, which can reduce corrosion resistance and lead to weld rejection in accordance with

* Corresponding author.
E-mail address: mohammad.jahazi@etsmtl.ca (M. Jahazi).

https://doi.org/10.1016/j.rinma.2025.100774
Received 2 April 2025; Received in revised form 21 August 2025; Accepted 1 October 2025
Available online 2 October 2025

standards such as AWS D18.1 and AWS D18.2 [4,5]. These standards impose strict limits on allowable oxidation levels for welds in corrosive service environments [5]. Therefore, understanding oxidation kinetics and the influence of trace oxygen levels is essential for predicting long-term performance and ensuring weld quality. Accurately assessing the oxidation kinetics of 316L at elevated temperatures is critical to mitigating such effects and preserving the integrity of welded structures.

Thermogravimetric analysis (TGA) is a powerful technique for studying the oxidation kinetics of metals and alloys. By measuring weight changes as a function of temperature, TGA provides insights into the oxidation rates and the formation of different oxide phases [6–9]. The data obtained from TGA can be further analyzed using isoconversional methods and model-fitting approaches to determine the activation energies and reaction mechanisms involved in the oxidation process [10]. Isoconversional methods offer a model-free approach to evaluating the kinetic parameters by examining the temperature dependence of the reaction rate at different degrees of conversion [11–13].These methods are advantageous as they do not require a predefined reaction model, thus providing a more accurate representation of the complex oxidation processes. The Friedman method, being a differential isoconversional technique, offers detailed kinetic information at each conversion level but is sensitive to experimental noise [13]. In contrast, FWO and KAS are integral methods that offer robustness against noise and are widely accepted for non-isothermal kinetic studies [11,12]. The Starink method was selected for its improved accuracy in calculating activation energy by correcting systematic errors associated with the temperature integral approximation used in KAS and FWO [10]. Various studies have successfully applied these methods to calculate the activation energy (E_a) for stainless steels and other high-temperature materials [14–16]. Model-fitting methods, including the Coats-Redfern and Kennedy-Clark methods, involve fitting experimental data to specific reaction models to extract kinetic parameters such as activation energies [17]. These methods can offer detailed insights into the reaction mechanisms by assuming a specific functional form for the reaction rate. Both methods were used to enhance the robustness of the kinetic analysis CR method provides a reliable estimation for ideal reaction behaviors, the KC method improves the fit for complex, multi-step reactions due to its refined approximation [17–19]. Using both allows cross-validation of the activation energy and better identification of the most representative solid-state reaction model. In Section 2.2, we provide more detail about all methods and related equations.

Thermogravimetric analysis (TGA) serves as an effective method for investigating the oxidation kinetics [6,8]. Cheng et al. [8] employed TGA to examine the oxidation behavior of Fe–10Cr steel in the temperature range of 1073–1273 K and determine the oxidation kinetics. The data obtained from TGA can be further analyzed using different methods, including isoconversional and model-fitting approaches to determine activation energy (E_a) and reaction models involved in the oxidation process [10]. Isoconversional methods provide a model-free strategy for assessing kinetic parameters by analyzing the temperature dependence of reaction rates at varying degrees of conversion (α) [11–13]. Each method has a distinct approach to determining E_a. The Friedman method, for instance, is a differential technique that determines the conversion rate at each point, making it highly sensitive to fluctuations in data or noise while offering detailed insights into reaction kinetics at specific conversion levels [13]. Conversely, the Flynn-Wall-Ozawa (FWO) as well as Kissinger-Akahira-Sunose (KAS) methods employ an integral approach, averaging reaction data over a wider range, improving stability against noise and yielding a more reliable estimate of activation energy [11,12,20,21]. The Starink method modifies the KAS approach to further minimize experimental errors [10]. Furthermore, research by Vázquez et al. identified the KAS method as the most effective of Cu_2S–FeS mixtures in an oxidative setting. This method demonstrated that activation energy varies significantly with conversion, validating a thermodynamic computational model that accurately replicates TGA curves [22]. While isoconversional methods offer a model-free approach to calculating E_a at various stages of the reaction, they do not provide detailed insights into specific reaction pathways. Therefore, the addition of non-isoconversional methods complements the analysis by offering more precise insights into the reaction models. The CR and KC methods, while both based on model-fitting techniques, differ in their assumptions and mathematical treatments. Both methods use a linearized form of the Arrhenius equation, where the natural log of the conversion function is represented in relation to the inverse of temperature. One limitation, however, is that it assumes a single dominant reaction mechanism, which may not always be applicable for complex reactions involving multiple stages [17,19,23]. KC employs a slightly different mathematical simplification than the CR method, allowing for more flexibility in fitting various types of kinetic data. This method is particularly useful when analyzing reactions with complex mechanisms, as it can account for multiple stages of the reaction process [15,18,23,24]. Various studies have successfully applied these methods to calculate the E_a [14–16]. Alhulaybi et al. [15] utilized TGA for investigating the pyrolysis kinetics of polylactic acid (PLA) at different heating rates, calculating activation energies through different model-free techniques (Friedman, FWO, KAS, and Starink) as well as model-fitting approaches (Coats-Redfern and Criado). Fernández et al. calculated the activation energy and pre-exponential factor (A) during the pyrolysis of walnut and almond shells using thermogravimetric analysis [25]. Model-fitting methods, involve fitting experimental data to specific reaction models to extract kinetic parameters such as E_a [17]. These methods can offer detailed insights into the reaction models by assuming a specific functional form for the reaction rate.

Additionally, some studies have calculated the E_a of 316L stainless steel after determining the parabolic rate constant (Kp) using TGA [26–28]. For instance, calculating the E_a for 316L stainless steel or similar alloys has been reported in the literature, providing valuable benchmarks for comparison. Studies have reported E_a values of 206 kJ/mol for 316LN stainless steels [26]. For 316L stainless steel plates, E_a values around 240 ± 20 kJ/mol have been observed within the temperature range of 973–1273 K [27]. The E_a in the 1073–1273 K temperature range has been calculated as 220 ± 30 kJ/mol [28]. In addition to kinetic modeling, the use of thermochemical software like FactSage allows for the simulation of high-temperature oxidation reactions and the prediction of stable phases and compounds [4]. Understanding these values and their variation across different temperature ranges is establishing a framework for oxidation kinetics.

Despite extensive research into the oxidation kinetics of 316L stainless steel, several gaps remain—particularly concerning the comprehensive application of advanced kinetic methodologies to understand high-temperature oxidation behavior. Most previous studies have relied on evaluating the parabolic rate constant (K_p) and deriving activation energy (E_a) indirectly, which may overlook the intricacies of multi-stage oxidation mechanisms and fail to accurately predict the associated solid-state reaction models [26–28]. Furthermore, while isoconversional and model-fitting methods have mostly been applied to polymers and non-metallic materials, their systematic integration for analyzing the oxidation kinetics of stainless steels remains limited.

To address these gaps, this study presents a novel and integrated kinetic–thermodynamic framework for evaluating the oxidation behavior of 316L stainless steel. Model-free isoconversional methods (FWO, KAS, Starink, and Friedman) were applied to calculate activation energies without assuming predefined reaction models, allowing for a precise assessment of oxidation behavior across varying degrees of conversion. Complementarily, model-fitting approaches such as Coats–Redfern (CR) and Kennedy–Clark (KC) were employed to identify reaction models and extract kinetic triplets (E_a, A, and f(α)). By applying both methods (isoconversional and model-fitting), we aimed to cross-validate the activation energies and gain a deeper understanding of the reaction mechanisms. To further refine the analysis, the Criado master plot method was used to identify the most suitable reaction

mechanisms by comparing theoretical and experimental reaction curves. By coupling kinetic modeling with thermochemical simulations via FactSage, this work presents a novel and comprehensive framework for understanding the high-temperature oxidation phenomena of 316L stainless steel in welding-related applications.

To the best of our knowledge, this is the first study to simultaneously apply multiple isoconversional and model-fitting methods to extract both kinetic and thermodynamic properties (E_a, A, anthalpy of activation ($\Delta H^{\neq}$), entropy of activation ($\Delta S^{\neq}$), and Gibbs energy of activation ($\Delta G^{\neq}$) to identify oxidation reaction models for 316L stainless steel. The originality of this work lies in its comprehensive approach, combining kinetic modeling, thermodynamic analysis, and reaction model prediction using both experimental TGA data and thermochemical simulations. This multi-faceted methodology offers a robust framework for understanding the high-temperature oxidation behavior of stainless steels (in the range of 1100–1373 K), with direct relevance to the complex oxidation phenomena induced by welding and other high-temperature industrial applications.

2. Material and methods

2.1. Preparation

The samples utilized for this study were supplied by PCL, Alberta Canada, with the chemical composition reported in Table 1. Prior to TGA experiments, the samples were polished and cleaned using ultrasonic cleaning in ethanol to eliminate surface contaminants and ensure consistency in the analysis.

TGA was conducted using a PerkinElmer STA 8000, United States. The instrument was calibrated for temperature according to the ASTM 967-18 standard using reference materials Bi_2O_3 and MgF_2, as detailed in Table 2. Each condition was repeated twice to determine two calibration points. Based on the standard, the Root Mean Square Error (RMSE) for our experiment was calculated as 4.65 K, ensuring the accuracy and reliability of the temperature measurements. Calibration before testing helps to minimize systematic errors and ensures high reliability of the measurements, even with a limited number of experimental runs [29–33].

Approximately 100 mg of material was used for each TGA run. The samples were placed in Alumina sample pans to ensure uniform heat distribution and avoid any reaction between the sample and the container. The TGA experiments were conducted under a continuous flow of high-purity argon gas (99.95 %) containing approximately 500 ppm (5×10^{-4} atm) of oxygen, at a flow rate of 50 ml/min. This condition was deliberately chosen to simulate the oxygen content typically present in industrial welding backing gas. Although argon is generally inert, this trace oxygen level induces high-temperature oxidation representative of the discoloration phenomenon observed in the HAZ during welding [4].

Heating rates of 25, 20, 15, 10, and 5 K/min were used covering one distinct temperature range (1100 K–1561 K) were used for the TGA experiments. These specific heating rates were chosen to explore the kinetics of oxidation across a broad spectrum of thermal conditions, allowing for a detailed analysis of the reaction models at both lower and higher heating rates. This range enables the application of isoconversional methods, which require multiple heating rates to determine reliable activation energies without assuming a specific reaction model [34]. Moreover, the use of lower heating rates allows the oxidation mechanisms to evolve more completely. The temperature ranges were chosen based on the DTG plot, that indicates different oxide formations occurring above 1100 K. The temperature-dependent weight loss of each sample was recorded.

Table 1
316L stainless steel chemical composition.

Element	C	Mo	Ni	Cu	S	P	Cr
wt.%	0.02	2.05	11.37	0.25	0.001	0.28	16.47
Element	Mn	Al	Co	Si	W	N	Others
wt.%	0.97	0.0162	0.22	0.43	0.073	0.093	0.13

Table 2
Calibration details for the TGA machine.

Material	Sample mass (mg)	Expected melting point (K)	Experimental average melting point (K)	β (K/min)	Ar gas flow (ml/min)
Bi_2O_3	80.6	1098	1095	10	50
MgF_2	46.2	1536	1527	10	50

2.2. Kinetic analysis

The activation energy was determined using several methods, as summarized in Table 3. In this paper, the Modified Friedman (MFR) method was employed for minimizing noise sensitivity inherent to the conventional Friedman approach [35]. Linear regression analysis was performed to determine the E_a from the slope of the plots. R^2 was used to assess the quality of the fit for each method. The results for isoconversional methods with R^2 values under 0.82 were excluded to maintain data reliability by eliminating poorly fitting models.

Based on the E_a and pre-exponential factor (A) obtained from both isoconversional and model-fitting methods, the thermodynamic properties of the oxidation process were calculated. The enthalpy of activation ($\Delta H^{\neq}$) was determined using the relation $\Delta H^{\neq} = E_a - RT$. The entropy of activation ($\Delta S^{\neq}$) was calculated using the Eyring equation [39–41]:

$$\Delta S^{\neq} = Rln\left(\frac{Ah}{k_B T}\right)$$

where R is the universal gas constant, h is Planck's constant (6.626×10^{-34} J s), k_B is Boltzmann's constant (1.381×10^{-23} J/K), and T is the absolute temperature.

The Gibbs energy of activation ($\Delta G^{\neq}$) was then calculated using [41]:

$$\Delta G^{\neq} = \Delta H^{\neq} - T\Delta S^{\neq}$$

Following the application of the CR and KC methods, the Criado method was employed to determine the solid-state reaction models [15]. The Criado plot involves plotting the reduced reaction rate against the extent of conversion to identify the most appropriate reaction model. In addition, to the Criado method, the methods reported by Alhulaybi et al. [28] and Agnihotri et al. [36] also conducted an investigation into reaction models at different conversion levels. The models included in the analysis are presented in Table 4. Using Equation (1), a conversion range of 0.1–0.7 was used for plotting experimental curves [15,36,38]:

$$\frac{Z(\alpha)}{Z(0.5)} = \left(\frac{T_\alpha}{T_{0.5}}\right)^2 \frac{\left(\frac{d\alpha}{dt}\right)_\alpha}{\left(\frac{d\alpha}{dt}\right)_{0.5}} \quad \text{(Equation 1)}$$

After determining the solid-state reaction model using the Criado method, FactSage thermochemical software (version 8.2, Ftstel and Ftoxid Database) was used to simulate the high-temperature reactions and identify the possible phases and compounds formed. The simulation inputs included the chemical composition of the investigated 316L stainless steel and examined temperature ranges. The FactSage analysis results were compared with experimental data to validate the reaction models and identify the predominant reactions occurring during the oxidation process. All data analyses and plots were generated using MATLAB R2022a.

Table 3
Summary of methods for Ea calculation [35–38].

Method	Type	Equation	Plot	Data analysis
Isoconversional				
Friedman	Differential	$Ln\left(\frac{d\alpha}{dt}\right) = \ln(A) - \frac{E_a}{RT}$	$ln(d\alpha/dt)$ *vs.* $1/T$	Slope gives E_a/R
M-Friedman	Differential	$Ln\left(\frac{d\alpha_{T_{k,i}}}{dt}\right) = \ln(A) - \frac{E_a}{RT_{k,i}}$	$ln\left(\frac{d\alpha_{T_{k,i}}}{dt}\right)$ *vs.* $1/T_{k,i}$	Slope gives E_a/R
FWO	Integral	$\ln(\beta) = \ln\left(\frac{A\,E_a}{Rg(\alpha)}\right) - 5.331 - 1.052\,\frac{E_a}{RT}$	$ln(\beta)$ *vs.* $1/T$	Slope gives $-1.052\ E_a/R$
KAS	Integral	$\ln\left(\frac{\beta}{T^2}\right) = \ln\left(\frac{A\,R}{E_a g(\alpha)}\right) - \frac{E_a}{RT}$	$ln(\beta/T^2)$ *vs.* $1/T$	Slope gives - E_a/R
Starink	Integral	$\ln\left(\frac{\beta}{T^{1.92}}\right) = \ln\left(\frac{AR}{E_\alpha^{0.92} g(\alpha)}\right) - \frac{1.0008E_a}{RT}$	$ln(\beta/T^{1.92})$ *vs.* $1/T$	Slope gives $-1.0008\ E_a/R$
Non- Isoconversional (Model- Fitting)				
KC	Differential	$\ln\left(\frac{\beta g(\alpha)}{T-T_0}\right) = \ln\left(\frac{A}{R}\right) - \frac{E_a}{RT}$	$ln(\beta g(\alpha)/(T-T_0))$ *vs.* $1/T$	Slope gives - E_a/R
CR	Integral	$\ln\left(\frac{g(\alpha)}{T^2}\right) = \ln\left(\frac{AR}{\beta E_a}\right) - \frac{E_a}{RT}$	$ln(g(\alpha)/T^2)$ *vs.* $1/T$	Slope gives - E_a/R

Table 4
Solid-state reaction models [36,42,43].

Nucleation Models	Model	
	Integral Form g(α) = kt	Differential Form f(α)
Avrami-Erofeev (A4)	$[-\ln(1-\alpha)]^{1/4}$	$4(1-\alpha)[-\ln(1-\alpha)]^{3/4}$
Avrami-Erofeev (A3)	$[-\ln(1-\alpha)]^{1/3}$	$3(1-\alpha)[-\ln(1-\alpha)]^{2/3}$
Avrami-Erofeev (A2)	$[-\ln(1-\alpha)]^{1/2}$	$2(1-\alpha)[-\ln(1-\alpha)]^{1/2}$
Power Law (P4)	$\alpha^{1/4}$	$4\alpha^{3/4}$
Power Law (P3)	$\alpha^{1/3}$	$3\alpha^{2/3}$
Power Law (P2)	$\alpha^{1/2}$	$2\alpha^{1/2}$
Geometrical Contraction Models		
Contracting Volume (R3)	$1-(1-\alpha)^{1/3}$	$3(1-\alpha)^{2/3}$
Contracting Area (R2)	$1-(1-\alpha)^{1/2}$	$2(1-\alpha)^{1/2}$
Diffusion Models		
Ginstling-Brounshtein (D4)	$1-2\alpha/3-(1-\alpha)^{2/3}$	$3[(1-\alpha)^{-1/3}-1]^{-1}$
3D Diffusion (D3)	$[1-(1-\alpha)^{1/3}]^2$	$3/2[(1-\alpha)^{-1/3}-1]$
2D Diffusion (D2)	$(1-\alpha)\ln(1-\alpha)+\alpha$	$[-\ln(1-\alpha)]^{-1}$
1D Diffusion (D1)	α^2	$1/(2\alpha)$
Reaction Order Models		
Third Order (F3)	$[1/(1-\alpha)^2]/2-1/2$	$(1-\alpha)^3$
Second Order (F2)	$[1/(1-\alpha)]-1$	$(1-\alpha)^2$
First Order (F1)	$-\ln(1-\alpha)$	$1-\alpha$
Zero Order (F0)	α	1

3. Results and discussion

3.1. Mass gain

The percentage weight gain in relation to temperature at various heating rates is depicted in Fig. 1. As the temperature increases, the sample begins to gain weight due to the formation of oxides. At 5 and 10 K/min (lower heating rates), the weight gain occurs gradually, with a more pronounced increase. This is because the slower heating rate allows more time for the oxidation reactions to occur uniformly across the sample's surface. At higher heating rates (15, 20 and 25 K/min), the weight gain is more rapid, and the curves are steeper. This indicates that the oxidation reactions are more vigorous, leading to a faster formation of oxides. However, the higher heating rate may result in less uniform oxidation, as the reactions are limited by the rapid temperature increase. The onset of weight gain typically starts around 1100 K, which aligns with the temperature range where significant oxidation reactions are expected based on DTG analysis, as reported in Fig. 2.

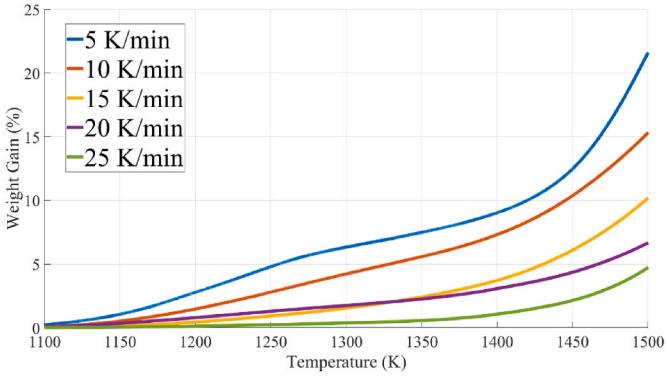

Fig. 1. The percentage weight gain of 316L stainless steel during heating at different rates.

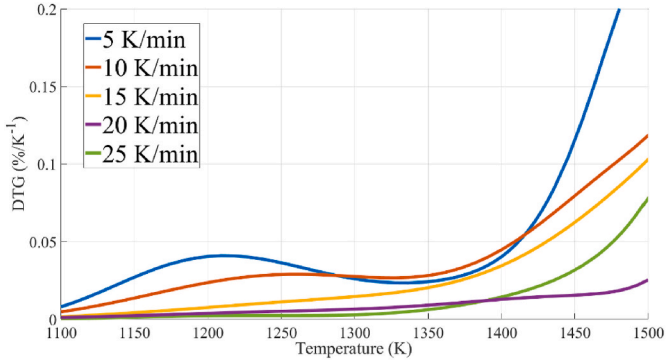

Fig. 2. DTG curves for different heating rates.

3.2. DTG and degree of conversion

The results of the DTG curves are presented in Fig. 2. As shown, the DTG curves reveal two distinct behaviors at two different temperature ranges (1100–1373 K and 1400–1500K). The peaks appear more pronounced at lowerheating rates due to the extended time for oxidation reactions to occur, allowing for better resolution of different oxidation events.

Fig. 3 displays the progression of oxidation in 316L stainless steel as a function of temperature, from 5 to 25 K/min heating rates by utilizing degree of conversion versus temperature. The curves demonstrate that the degree of conversion increases more steeply as the temperature

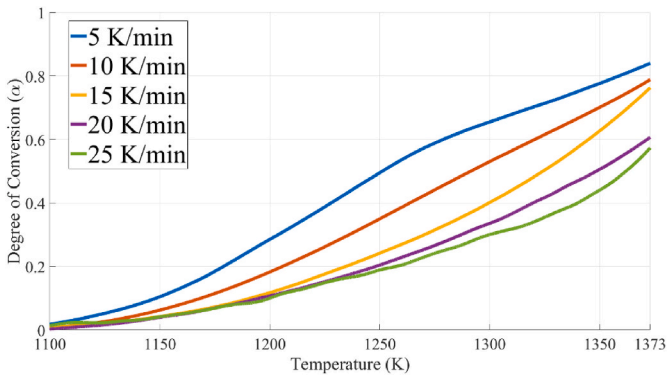

Fig. 3. Variation in the relationship between the degree of conversion and temperature at various heating rates.

approaches higher values. This behavior indicates that the oxidation process accelerates at higher temperatures, with faster heating rates leading to quicker attainment of similar degrees of conversion.

3.3. Isoconversional kinetic models

As reported in Table 3, several isoconversional methods, including M-Friedman, FWO, KAS and Starink were employed in the present work.

On the basis of the data reported in Fig. 4, the activation energy values were calculated and are reported in Table 5 along with the corresponding R^2 coefficients. While slight variations in E_a could be observed between the methods, the consistency across them validates the reliability of the kinetic parameters. For instance, at a α of 0.5, the E_a values for FWO, KAS, Starink and Friedman methods are 190.49 kJ/mol, 178.7 kJ/mol, 179.42 kJ/mol, and 226.71 kJ/mol, respectively, with R^2 values indicating a good fit for all methods. The higher activation energy value estimated when using M-Friedman method could be related to the differential nature, i.e., derivative based equations, of this method. As reported in Table 5, E_a values for the M-Friedman method oscillate between 104.13 and 825.7 kJ/mol with R^2 values between 0.31 and 0.99, demonstrating the sensitivity of the method to changes in the conversion value. Therefore, the value obtained using the M-Friedman method will not be considered in the Following sections.

The thermodynamic properties calculated from different isoconversional methods offer crucial insights into the oxidation mechanism of 316L stainless steel. As shown in Table 6, $\Delta H^{\neq}$ values obtained from the FWO, KAS, Starink, and Friedman methods averaged 224.42, 214.14, 214.99, and 259.75 kJ/mol, respectively, indicating consistency across integral and differential approaches. The corresponding $\Delta G^{\neq}$ values were also closely aligned, averaging 252.97, 285.38, 285.43, and 286.19 kJ/mol. This agreement validates the robustness of the calculated kinetic parameters. Notably, the entropy of activation showed negative values for most methods suggesting a transition state with reduced disorder compared to the reactants, which is typical in solid-state diffusion-controlled processes. The positive $\Delta S^{\neq}$ values at low α and high α reflect the increasing complexity and possible multistep nature of the oxidation reaction at those conversion levels. These thermodynamic trends further confirm the progressive formation of protective oxide scales and the complex nature of the oxidation mechanism, as supported by the kinetic model fitting and phase transformation analysis.

Fig. 5 shows the average E_a value from different Isoconversional methods examined in the present work, as reported in Table 3. It is important to note that values for 0.8, 0.9 for all methods and 0.1 degrees of conversion for M-Friedman were excluded due to their low R^2, which indicated a poor fit. The M-Friedman method, being a differential approach, exhibits higher sensitivity to experimental noise, leading to slight variations in activation energy values [35].

E_a in relation to α for various isoconversional methods is illustrated in Fig. 6. In the initial phase of the oxidation process (α = 0.1 to 0.4), it is observed that there is a slight decrease in the E_a value in FWO, KAS and Starink. This trend is likely due to the initial development of oxide layers forming on the sample's surface. During this phase, the reaction is likely dominated by the nucleation and initial growth of oxide nuclei, which require relatively higher energies [44]. As these nuclei grow and coalesce, the energy barrier decreases slightly, facilitating further oxidation [44]. From α = 0.4 to 0.7, a steady increase is observed in the E_a value, with a similar slope across all methods. This phase corresponds to the thickening and densification of the oxide layer [45–47]. As the oxide

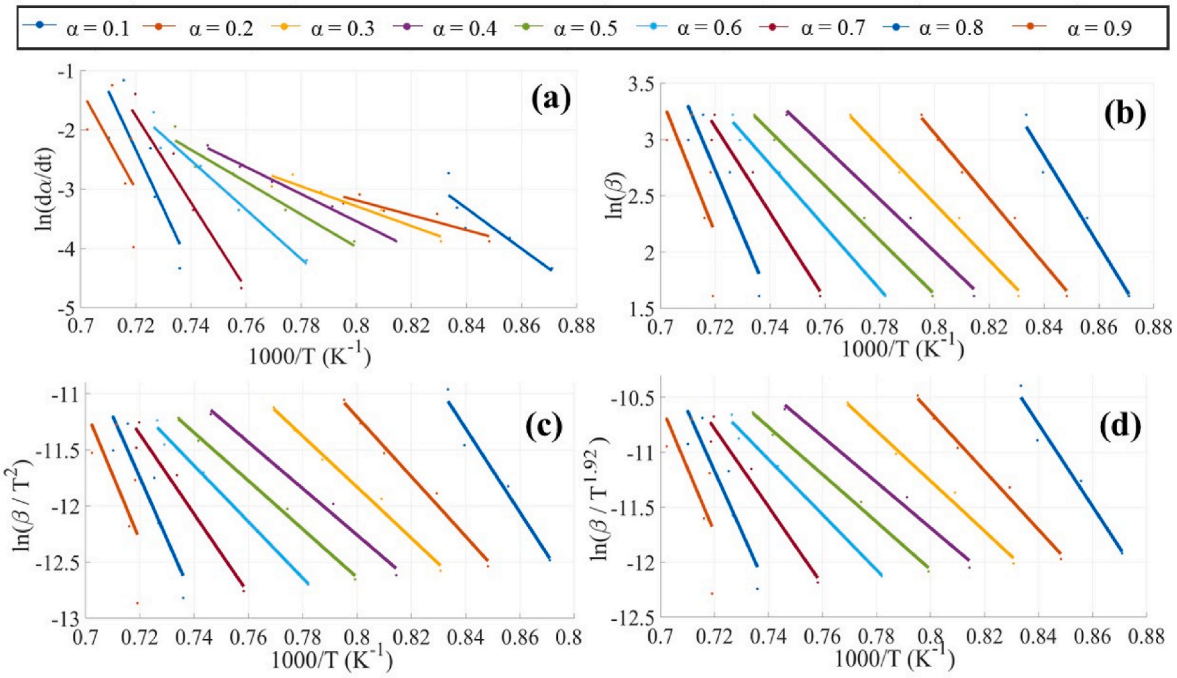

Fig. 4. Isoconversional plots for Ea determination; a) M-Friedman, b) FWO, c) KAS, and d) Starink.

Table 5
E_a (kJ/mol) , Ln(A)(1/S) and R^2 values determined using various isoconversional methods for different α values.

α	Method											
	FWO			KAS			Starink			M-Friedman		
	E_a	Ln (A)	R^2	E_a	Ln (A)	R^2	E_a	Ln (A)	R^2	E_a	Ln (A)	R^2
0.1	313.88	36.95	0.97	310.68	35.27	0.97	311.21	35.35	0.97	282.43	32.49	0.81
0.2	229.4	28.28	0.99	221.08	25.74	0.99	221.72	25.82	0.99	104.13	15.01	0.84
0.3	199.23	25.203	0.99	188.8	22.28	0.99	189.48	22.35	0.99	138.56	17.79	0.91
0.4	183.21	23.58	0.99	171.43	20.37	0.99	172.14	20.45	0.99	189.91	21.99	0.99
0.5	190.49	24.32	1	178.7	20.73	1	179.42	20.80	1	226.71	24.88	0.94
0.6	218.78	27.19	0.99	208.09	22.97	0.99	208.8	23.04	0.99	345.08	34.77	0.96
0.7	301.68	35.70	0.97	294.81	29.98	0.96	290	30.06	0.96	606.06	56.74	0.91
0.8	454.7	51.60	0.82	455.34	43.13	0.82	455.9	43.21	0.82	825.7	74.73	0.71
0.9	482.24	54.47	0.44	483.92	45.04	0.41	484.46	45.12	0.41	700.87	63.29	0.31

Table 6
$\Delta H^{\neq}$ (kJ/mol), $\Delta S^{\neq}$ (J/mol) and $\Delta G^{\neq}$ (kJ/mol) values determined using various isoconversional methods for different α values.

α	Method											
	FWO			KAS			Starink			M-Friedman		
	$\Delta H^{\neq}$	$\Delta S^{\neq}$	$\Delta G^{\neq}$	$\Delta H^{\neq}$	$\Delta S^{\neq}$	$\Delta G^{\neq}$	$\Delta H^{\neq}$	$\Delta S^{\neq}$	$\Delta G^{\neq}$	$\Delta H^{\neq}$	$\Delta S^{\neq}$	$\Delta G^{\neq}$
0.1	304.49	43.03	255.93	300.87	28.56	267.14	301.65	29.2	267.17	272.61	5.43	266.21
0.2	220.01	−29.21	252.98	210.9	−50.96	273.33	211.71	−50.33	273.37	93.94	−140.18	265.66
0.3	189.85	−54.76	251.66	178.33	−80	279.08	179.16	−79.37	279.13	128.09	−117.31	275.84
0.4	173.83	−68.26	250.87	160.7	−96.05	284.63	161.55	−95.43	284.68	179.18	−82.57	285.73
0.5	181.1	−62.13	251.24	167.76	−93.24	290.41	168.63	−92.62	290.46	215.78	−58.71	293.01
0.6	209.4	−38.22	252.54	196.96	−74.75	297.01	197.84	−74.13	297.06	333.95	23.39	302.64
0.7	292.29	32.55	255.55	283.49	−16.58	306.07	284.39	−15.94	306.11	594.73	205.87	314.24
Average	224.42	−25.29	252.97	214.14	−54.72	285.38	214.99	−54.09	285.43	259.75	−23.44	286.19

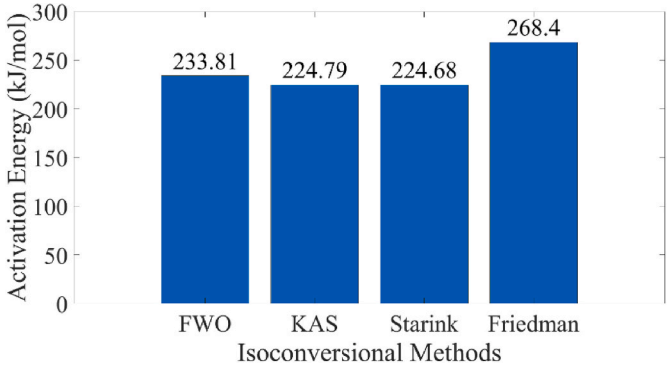

Fig. 5. Average E_a from isoconversional methods.

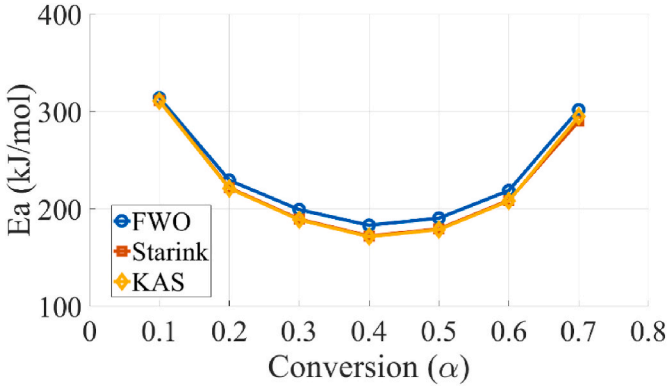

Fig. 6. E_a as a function of α using various isoconversional methods.

layer grows, diffusion of oxygen and metal ions through the oxide becomes the rate-limiting factor. This diffusion-controlled process requires higher E_a, which accounts for the observed increase [46].

3.4. Model-fitting kinetics methods

Table 7 presents the E_a values obtained by CR method for 15 different reaction models for the heating rates used in the present work.

After plotting the experimental data, they were fitted to a linear model using MATLAB. The high R^2 values (ranging from 0.961 to 0.989) demonstrate a strong correlation between the model and experimental data, supporting the validity of using a linear model to determine E_a.

By comparing the obtained E_a. values with those from the isoconversional methods, the most plausible reaction models were identified. When comparing the E_a values from the CR and KC methods with those obtained through isoconversional methods, as presented in Tables 7 and 8 and Fig. 7, it is evident that the F2 (second-order) and F3 (third-order) reaction models, with Ea values ranging between 203.2 kJ/mol and 239.5 kJ/mol, present a good agreement with the isoconversional averages, which range between 224.79 kJ/mol and 268.41 kJ/mol. This finding indicates that these reaction models effectively represent the oxidation kinetics of 316L stainless steel. The close alignment with the isoconversional methods suggests that both the F2 and F3 models are appropriate for describing the formation and growth of oxide layers during oxidation, particularly in capturing the complex mechanisms of spinel and corundum formation at different stages of the process.

3.5. Criado method analysis

The Criado master plots shown in Fig. 7 help identify the most appropriate reaction models that closely align with the experimental data. As shown, the normalized reaction rates (Z(α)/Z(0.5)) are plotted against the extent of α for various heating rates used in this study.

As shown in Fig. 7, at higher heating rates, the oxidation kinetics of 316L stainless steel transition from being reaction-controlled to

Table 7
E_a (kJ/mol) values obtained by the CR model.

Reaction Model	Heating rate (K/min)										Average	
	5		10		15		20		25			
	E_a	R^2	E_a	R^2	E_a	R^2	E_a	R^2	E_a	R^2	E_a	R^2
D1	316.4	0.926	372.4	0.943	377.1	0.976	311.6	0.976	317	0.981	338.9	0.961
D2	336.7	0.939	387.7	0.951	387.5	0.98	322.8	0.98	323.9	0.983	351.7	0.967
D3	359.6	0.951	404.1	0.959	399.1	0.983	334.3	0.984	331.2	0.985	365.7	0.973
D4	−70.5	0.992	−59.8	0.979	−47.7	0.969	−48.8	0.977	−40.6	0.984	−53.5	0.98
F0	148.1	0.916	176.3	0.936	178.5	0.973	145.5	0.973	148.6	0.978	159.4	0.955
F1	181.6	0.957	200.5	0.963	195.1	0.985	163	0.985	158.9	0.985	179.8	0.975
F2	221.6	0.983	228.2	0.981	213.5	0.993	182.3	0.993	170.2	0.99	203.2	0.988
F3	268	0.996	259.3	0.992	233.7	0.997	203.8	0.997	182.2	0.994	229.4	0.995
P2	63.99	0.889	78.09	0.919	79.15	0.965	62.59	0.962	64.25	0.97	69.62	0.941
P3	35.94	0.847	45.34	0.894	46.05	0.953	34.87	0.944	36.14	0.957	39.67	0.919
P4	21.94	0.782	28.96	0.857	29.5	0.935	21.01	0.913	22.08	0.935	24.7	0.885
A2	80.73	0.944	90.18	0.953	87.49	0.98	71.2	0.98	69.43	0.98	79.8	0.968
A3	47.12	0.927	53.4	0.94	51.61	0.974	40.61	0.972	39.7	0.972	46.49	0.957
A4	30.3	0.901	35.01	0.921	33.66	0.965	25.31	0.958	24.75	0.958	29.81	0.941
R2	164.1	0.938	188	0.95	186.6	0.979	154.1	0.979	153.7	0.982	169.3	0.966
R3	169.7	0.945	191.9	0.955	189.5	0.981	156.9	0.982	155.6	0.983	172.7	0.969

Table 8
E_a (kJ/mol) values obtained using the KC model.

Reaction Model	Heating rate (K/min)										Average	
	5		10		15		20		25			
	E_a	R^2	E_a	R^2	E_a	R^2	E_a	R^2	E_a	R^2	E_a	R^2
D1	326.5	0.931	382.5	0.946	387.2	0.978	321.9	0.978	327.1	0.983	349	0.963
D2	346.8	0.942	397.8	0.954	397.6	0.981	333.1	0.982	333.9	0.985	361.8	0.969
D3	369.7	0.954	414.1	0.961	409.2	0.984	344.6	0.985	341	0.986	375.7	0.974
D4	−60.4	0.99	−49.8	0.972	−37.6	0.954	−38.6	0.966	−30.6	0.974	−43.4	0.971
F0	158.2	0.926	186.2	0.943	188.5	0.976	155.8	0.976	158.5	0.981	169.5	0.961
F1	191.7	0.961	210.6	0.966	205.2	0.986	173.3	0.987	169	0.987	190	0.978
F2	231.7	0.984	238.1	0.983	223.6	0.994	192.6	0.994	180.2	0.992	213.3	0.989
F3	278.1	0.996	269.4	0.993	243.8	0.998	214.2	0.997	192.2	0.995	239.5	0.996
P2	74.07	0.916	88.17	0.936	89.23	0.973	72.76	0.973	74.3	0.978	79.71	0.955
P3	46.02	0.904	55.42	0.928	56.13	0.969	45.08	0.968	46.18	0.975	49.77	0.949
P4	31.99	0.889	39.04	0.919	39.58	0.965	31.3	0.962	32.13	0.97	34.81	0.941
A2	90.81	0.957	100.3	0.963	97.57	0.985	81.49	0.985	79.47	0.985	89.92	0.975
A3	57.18	0.951	63.48	0.958	61.69	0.983	50.89	0.983	49.63	0.983	56.58	0.972
A4	40.36	0.944	45.09	0.953	43.75	0.98	35.6	0.98	34.71	0.98	39.9	0.968
R2	174.2	0.945	197.9	0.956	196.7	0.982	164.4	0.982	163.8	0.984	179.4	0.97
R3	179.8	0.951	202	0.959	199.5	0.983	167.2	0.984	165.6	0.985	182.8	0.973

diffusion-controlled due to the interplay of reaction rates and diffusion limitations. While lower heating rates allow for the formation of thicker and more uniform oxide layers, the slower reaction rate ensures that diffusion does not become the rate-limiting step, leading to reaction-order kinetics dominated by models such as F1, F2, and F3. In contrast, higher heating rates (e.g., 20 and 25 K/min) lead to rapid temperature increases, causing the oxide layer to form more quickly but less uniformly. This rapid growth creates a scenario where the supply of oxygen or metal ions through the oxide layer cannot keep pace with the reaction at the metal-oxide interface, resulting in diffusion-controlled kinetics. Specifically, D1 dominates at 20 K/min, while at 25 K/min, the oxide morphology becomes more complex, favoring two-dimensional diffusion D2 through lateral pathways such as grain boundaries or pores.

3.6. Oxidation of 316L stainless steel below 1373 K

Thermochemical results obtained using FactSage showed that at 1073 K, the primary oxides formed include spinel and corundum, as shown in Equations (2) and (3), respectively. Spinel in this context likely contains chromium and iron oxides and corundum includes chromium and iron oxides in this alloy [4].

Spinel Formation : $Fe_3O_4(magnetite) + Cr_2O_3 \rightarrow (Fe, Cr)_3O_4$ Equation 2

Corundum Formation : $Fe_2O_3(Hematite) + Cr_2O_3 \rightarrow (Fe, Cr)_2O_3$ Equation 3

The oxidation of 316L stainless steel begins with the formation of iron oxides and chromium oxides on the surface [48].

Formation of Iron Oxide : $Fe + \frac{1}{2}O_2 \rightarrow FeO$ Equation 4

$2FeO + \frac{1}{2}O_2 \rightarrow Fe_2O_3$ Equation 5

Formation of Chromium Oxide : $Cr + \frac{3}{2}O_2 \rightarrow Cr_2O_3$ Equation 6

These simulations modeled oxide formation in 316L stainless steel under various oxygen partial pressures and temperature ranges representative of welding conditions. The predictions revealed a duplex oxide scale composed of an inner corundum layer ($(Fe,Cr)_2O_3$) and an outer spinel phase ($(Fe,Cr)_3O_4$), consistent with the elemental mapping and kinetic behavior observed in the present study. These thermochemical predictions align with the experimental observations of Maroufkhani et al. [4], who reported a duplex oxide structure with an inner Cr-rich layer and an outer Fe-rich oxide layer near the fusion zone of welded 316L stainless steel, validating the progressive oxidation mechanism.

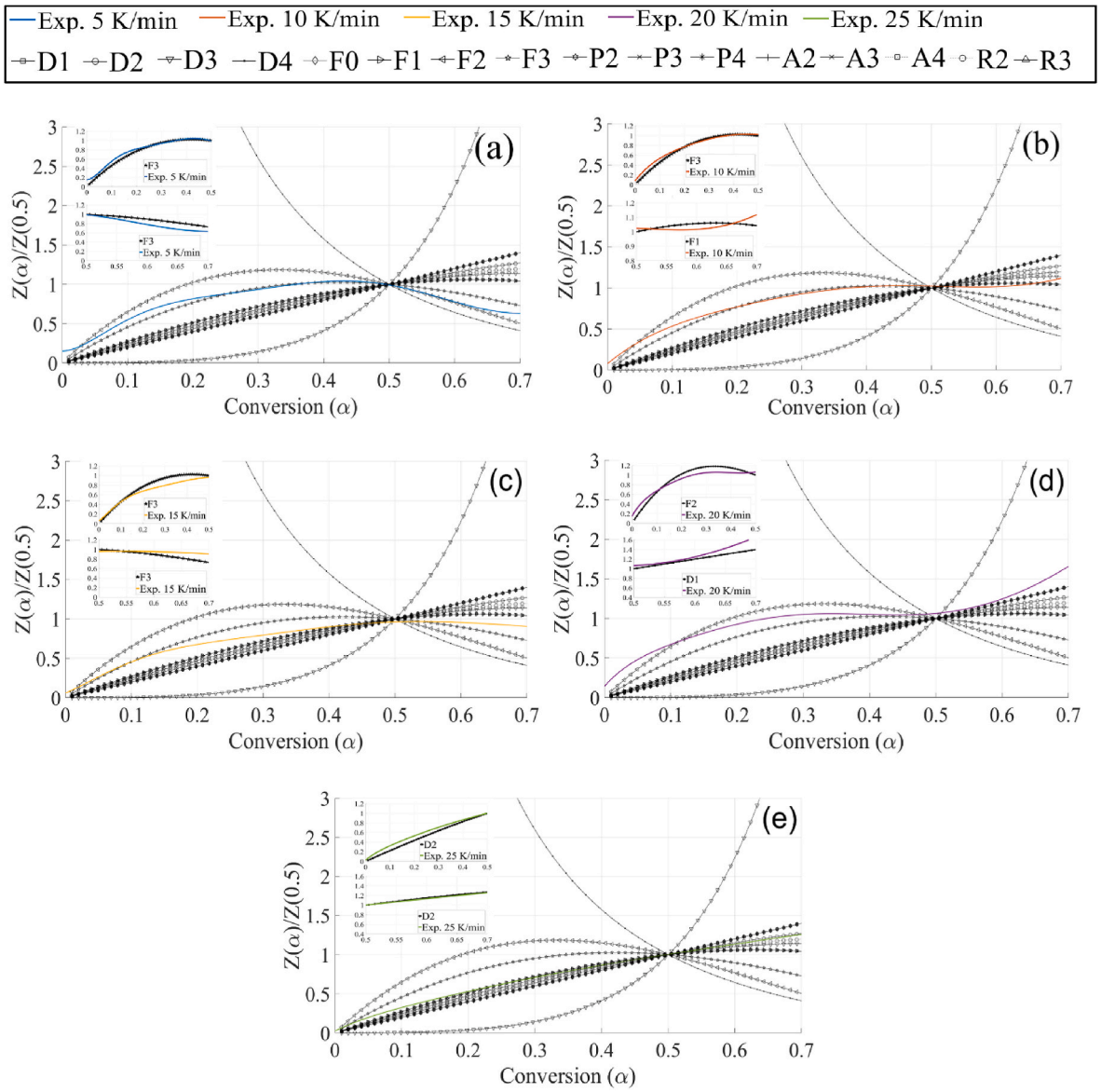

Fig. 7. Criado master plots for low temperature tests with different β: a) 5, b)10, c)15, d)20, e)25 K/min.

The presence of spinel and corundum phases in both the FactSage results and experimental EDS mapping supports the stepwise oxidation kinetics observed in this study, further justifying the reaction models (F2, F3) derived from kinetic analysis. These previously validated results are briefly incorporated in the current manuscript to reinforce the correlation between calculated phase stability and the experimental oxidation pathways under TGA conditions.

The composition and structure of the protective oxide layer are critical in determining the oxidation resistance of 316L stainless steel. Typically, a duplex oxide scale forms, consisting of an inner chromium-rich corundum phase (Cr_2O_3 or $(Fe,Cr)_2O_3$) and an outer iron-rich spinel phase ($(Fe,Cr)_3O_4$). The inner corundum layer acts as a dense barrier, effectively limiting the diffusion of oxygen and metal ions, thereby enhancing corrosion resistance [49]. In contrast, the outer spinel layer, while less dense, accommodates defects and aids in stress relaxation, improving the adhesion of the oxide scale during thermal cycling [50]. This synergistic combination of corundum and spinel phases contributes to the overall protective nature of the oxide layer [51]. These findings are consistent with the observations reported by Maroufkhani et al., who identified a duplex oxide structure with an inner Cr-rich layer and an outer Fe-rich oxide layer near the fusion zone of welded 316L stainless steel [4].

3.6.1. *Reactions for F2 and F3 models*

The F2 model suggests that the oxidation rate is directly proportional to the square of the remaining unreacted material. The F3 model, also fitting well with experimental data, indicates that the oxidation rate is proportional to the cube of the amount of unreacted material. This suggests an even more complex mechanism involving rapid nucleation and growth of multiple oxide layers. By following both F2 and F3 models, this study offers a detailed understanding of the oxidation mechanisms in 316L stainless steel. There is a possibility that both models correspond to the formation of spinel and corundum.

Further investigation into the microstructural evolution beneath the oxide scale, including grain boundary effects and oxidation-induced transformations, is planned as a future extension of this research.

4. Conclusions

This study examined the oxidation kinetics of 316L stainless steel using both isoconversional and non-isoconversional methods. The main findings and their implications are summarized below.

1. The E_a from the CR and KC methods were compared with isoconversional methods. The second and third order (F2 and F3) reaction models were identified as the most accurate ones representing the oxidation process of 316L stainless steel at temperatures below 1373 K, and Criado plot analysis confirmed that the F2 and F3 models align closely with experimental data across different heating rates.
2. The FWO, KAS and Starink isoconversional methods provided average E_a values of 233.81 kJ/mol, 224.79 kJ/mol and 224.68 kJ/mol, respectively, which are consistent with those obtained from the CR and KC methods, ranging between 203.2 kJ/mol and 239.5 kJ/mol.
3. The thermodynamic properties were calculated using FWO, KAS, Starink, and Friedman methods. The average $\Delta H^{\neq}$ values ranged from 214.14 to 224.42 kJ/mol, average $\Delta S^{\neq}$ values ranged from −54.72 to −23.44 J/mol·K, and average $\Delta G^{\neq}$ values ranged from 252.97 to 286.19 kJ/mol. The negative $\Delta S^{\neq}$ values reflect a more ordered transition state, which is typical for solid-state oxidation reactions.
4. FactSage simulations and experimental data confirmed the formation of spinel (containing Fe-Cr oxides) and corundum (Fe_2O_3-Cr_2O_3 structures) as the primary oxides at temperatures below 1100 K.

CRediT authorship contribution statement

Mohammad Maroufkhani: Writing – original draft, Visualization, Software, Project administration, Methodology, Formal analysis, Data curation, Conceptualization. **Alireza Khodabandeh:** Writing – review & editing, Visualization, Supervision, Methodology, Conceptualization. **Iulian Radu:** Supervision. **Elmira Moosavi-Khoonsari:** Writing – review & editing, Validation, Formal analysis. **Mohammad Jahazi:** Writing – review & editing, Visualization, Supervision, Project administration.

Declaration of competing interest

The authors declare the following financial interests/personal relationships which may be considered as potential competing interests: Mohammad maroufkhani reports financial support was provided by Natural Sciences and Engineering Research Council of Canada. Iulian Radu reports a relationship with PCL Inc that includes: employment. If there are other authors, they declare that they have no known competing financial interests or personal relationships that could have appeared to influence the work reported in this paper.

Acknowledgment

This research was conducted in partnership with PCL Construction in Edmonton, which provided the study materials, and was supported by funding from the Natural Sciences and Engineering Research Council of Canada (NSERC) under Grant No. RDC 542299-19. Special thanks to Saleh Rasouli for his assistance with the calibration process.

Data availability

The data that has been used is confidential.

References

[1] S. Hakimian, et al., Application of machine learning for the classification of corrosion behavior in different environments for material selection of stainless steels, Comput. Mater. Sci. 228 (2023) 112352, https://doi.org/10.1016/j.commatsci.2023.112352.
[2] T. Dudziak, et al., Effect of 316L stainless steel fabrication on oxidation resistance, surface morphology, and hot tensile behavior, J. Mater. Eng. Perform. 32 (22) (2023) 10443–10454, https://doi.org/10.1007/s11665-023-08321-6.
[3] A.J. Sedriks, Corrosion of Stainless Steels, 2001.
[4] M. Maroufkhani, et al., Influence of oxygen content in the protective gas on pitting corrosion resistance of a 316l stainless steel weld joint, Materials 16 (17) (2023) 5968, https://doi.org/10.3390/ma16175968.
[5] R.E. Avery, Sanitary welding standards, in: ASME Citrus Engineering Symposium, American Society of Mechanical Engineers, 2000, https://doi.org/10.1115/CEC2000-4605.
[6] C. De Blasio, C. De Blasio, Thermogravimetric analysis (TGA), Fundament. Biofuel. Eng. Technol. (2019) 91–102.
[7] M. Fatahiamirdehi, et al., Enhancing corrosion resistance of 316L stainless steel through electrochemical deposition of polyaniline coatings in acidic environments, J. Mater. Sci. (2024) 1–12.
[8] L. Cheng, et al., High-temperature oxidation behavior of Fe–10Cr steel under different atmospheres, Materials 14 (13) (2021) 3453, https://doi.org/10.3390/ma14133453.
[9] S. Vyazovkin, Computational aspects of kinetic analysis.: part C. The ICTAC kinetics project—the light at the end of the tunnel? Thermochim. Acta 355 (1–2) (2000) 155–163.
[10] M. Starink, The determination of activation energy from linear heating rate experiments: a comparison of the accuracy of isoconversion methods, Thermochim. Acta 404 (1–2) (2003) 163–176, https://doi.org/10.1016/S0040-6031(03)00144-8.
[11] J.H. Flynn, L.A. Wall, General treatment of the thermogravimetry of polymers, J. Res Natl Bur Stand Sect A, Phys. Chem 70 (6) (1966) 487, https://doi.org/10.6028/jres.070A.043.
[12] H.E. Kissinger, Reaction kinetics in differential thermal analysis, Anal. Chem. 29 (11) (1957) 1702–1706, https://doi.org/10.1021/ac60131a045.
[13] H.L. Friedman, Kinetics of thermal degradation of char-forming plastics from thermogravimetry. Application to a phenolic plastic, in: Journal of Polymer Science Part C: Polymer Symposia, Wiley Online Library, 1964, https://doi.org/10.1002/polc.5070060121.
[14] M. Brown, et al., Computational aspects of kinetic analysis: part A: the ICTAC kinetics project-data, methods and results, Thermochim. Acta 355 (1–2) (2000) 125–143, https://doi.org/10.1016/S0040-6031(00)00443-3.
[15] Z. Alhulaybi, et al., Pyrolysis kinetic study of polylactic acid, Polymers 15 (1) (2022) 12, https://doi.org/10.3390/polym15010012.
[16] S. Demirci, et al., Non-isothermal kinetic analysis of high temperature oxidation of additively manufactured Ti-6Al-4V alloy, J. Mater. Eng. Perform. (2024) 1–12, https://doi.org/10.1007/s11665-024-09557-6.
[17] A.W. Coats, J. Redfern, Kinetic parameters from thermogravimetric data, Nature 201 (4914) (1964) 68–69, https://doi.org/10.1038/201068a0.
[18] J. Kennedy, S. Clark, A new method for the analysis of non-isothermal DSC and diffraction data, Thermochim. Acta 307 (1) (1997) 27–35, https://doi.org/10.1016/S0040-6031(96)02962-0.
[19] A. Coats, J. Redfern, Kinetic parameters from thermogravimetric data. II, J. Polym. Sci. B Polym. Lett. 3 (11) (1965) 917–920, https://doi.org/10.1002/pol.1965.110031106.
[20] T. Akahira, Trans. Joint convention of four electrical institutes, Res. Rep. Chiba Inst. Technol. 16 (1971) 22–31.
[21] Q. Huang, et al., Study on the high temperature oxidation/nitridation behavior of Mg alloys AZ31, WE43 and ZE10, Case Stud. Therm. Eng. 30 (2022) 101759.
[22] M.V. Vázquez, et al., Kinetic study of Cu2S–FeS mixtures in an oxidative environment by thermogravimetric and thermodynamic analysis, Mater. Chem. Phys. 311 (2024) 128548, https://doi.org/10.1016/j.matchemphys.2023.128548.
[23] X. Gao, et al., Thermal kinetics and reactive mechanism of cellulose nitrate decomposition by traditional multi kinetics and modeling calculation under isothermal and non-isothermal conditions, Ind. Crop. Prod. 145 (2020) 112085, https://doi.org/10.1016/j.indcrop.2020.112085.
[24] V. Sugumaran, A. Kamalakkannan, B. Subramanian, Extricating the effect of sodium monovalent cation in the crystallization kinetics of bioactive glass and its influence on bioactivity, Mater. Chem. Phys. 305 (2023) 127897, https://doi.org/10.1016/j.matchemphys.2023.127897.
[25] A. Fernandez, et al., Assessment of the use of biochar from the slow pyrolysis of walnut and almond shells as an energy carrier, Energy Sources, Part A Recovery, Util. Environ. Eff. 46 (1) (2024) 15379–15394.
[26] S.İ. Ayvaz, İ. Aydın, A.İ. Bahcepınar, Effect of shot blasting on the boriding kinetics of AISI 316L stainless steel, Protect. Met. Phys. Chem. Surface 59 (4) (2023) 671–678, https://doi.org/10.1007/s11665-024-09557-6.
[27] C. Siri, et al., Impact of selective laser melting additive manufacturing on the high temperature behavior of AISI 316L austenitic stainless steel, Oxid. Metals 94 (2020) 527–548, https://doi.org/10.1007/s11085-020-10005-8.
[28] H. Buscail, et al., Effect of pre-oxidation at 800° C on the pitting corrosion resistance of the AISI 316L stainless steel, Oxid. Metals 75 (1) (2011) 27–39, https://doi.org/10.1007/s11085-010-9218-2.
[29] M. Almaghrabi, et al., Evaluating thermogravimetric analysis for the measurement of drug loading in mesoporous silica nanoparticles (MSNs), Thermochim. Acta 730 (2023) 179616.
[30] W. Xu, et al., Fundamentals of TGA and SDT, 2005.
[31] N. Saadatkhah, et al., Experimental methods in chemical engineering: thermogravimetric analysis—Tga, Can. J. Chem. Eng. 98 (1) (2020) 34–43.
[32] M.A. Siddiqi, R.A. Siddiqui, B. Atakan, Thermal stability, sublimation pressures and diffusion coefficients of some metal acetylacetonates, Surf. Coating. Technol. 201 (22–23) (2007) 9055–9059.
[33] B. Fazlioglu-Yalcin, M. Hilse, R. Engel-Herbert, Thermogravimetric study of metal–organic precursors and their suitability for hybrid molecular beam epitaxy, J. Mater. Res. 39 (3) (2024) 436–448.

[34] A. Rajabi, A. Mashreghi, S. Hasani, Non-isothermal kinetic analysis of high temperature oxidation of Ti–6Al–4V alloy, J. Alloys Compd. 815 (2020) 151948.
[35] J.A. Huidobro, et al., Reducing the effects of noise in the calculation of activation energy by the Friedman method, Chemometr. Intell. Lab. Syst. 151 (2016) 146–152, https://doi.org/10.1016/j.chemolab.2015.12.012.
[36] N. Agnihotri, M.K. Mondal, Thermal analysis, kinetic behavior, reaction modeling, and comprehensive pyrolysis index of soybean stalk pyrolysis, Biomass Conversion and Biorefinery (2023) 1–16, https://doi.org/10.1007/s13399-023-03807-8.
[37] B. Gajera, et al., Pyrolysis of cattle manure: kinetics and thermodynamic analysis using TGA and artificial neural network, Biomass Convers. Biorefine. (2023) 1–17, https://doi.org/10.1007/s13399-023-04476-3.
[38] P. Sharma, P. Diwan, O. Pandey, Impact of environment on the kinetics involved in the solid-state synthesis of bismuth ferrite, Mater. Chem. Phys. 233 (2019) 171–179, https://doi.org/10.1016/j.matchemphys.2019.05.055.
[39] Y. He, et al., Thermal decomposition and kinetics of coal and fermented cornstalk using thermogravimetric analysis, Bioresour. Technol. 259 (2018) 294–303.
[40] C.T. Chong, et al., Pyrolysis characteristics and kinetic studies of horse manure using thermogravimetric analysis, Energy Convers. Manag. 180 (2019) 1260–1267.
[41] S. Vyazovkin, Misinterpretation of thermodynamic parameters evaluated from activation energy and preexponential factor determined in thermal analysis experiments, Thermoelectrics 4 (3) (2024) 373–381.
[42] N. Khattar, et al., Optimization of compression parameters of UHMWPE through thermal stability, Mater. Chem. Phys. 307 (2023) 128220, https://doi.org/10.1016/j.matchemphys.2023.128220.
[43] Y. Yang, et al., Effect of metal chloride on thermal decomposition of nitrocellulose, Case Stud. Therm. Eng. 28 (2021) 101667.
[44] T. Brylewski, J. Dąbek, K. Przybylski, Oxidation kinetics study of the iron-based steel for solid oxide fuel cell application, J. Therm. Anal. Calorim. 77 (2004) 207–216, https://doi.org/10.1023/B:JTAN.0000033205.69427.8e.
[45] F.P. Fehlner, N.F. Mott, Low-temperature oxidation, Oxid. Metals 2 (1) (1970) 59–99, https://doi.org/10.1007/BF00603582.
[46] D.J. Young, High Temperature Oxidation and Corrosion of Metals, 1, Elsevier, 2008.
[47] Z. Chen, et al., The effects of temperature and oxygen pressure on the initial oxidation of stainless steel 441, Int. J. Hydrogen Energy 39 (19) (2014) 10303–10312, https://doi.org/10.1016/j.ijhydene.2014.04.188.
[48] P. Hou, 1.10 Oxidation of Metals and Alloys, 2010.
[49] A. Van Der Geest, et al., Energy ordering of grain boundaries in Cr2O3: insights from theory, J. Phys. Condens. Matter 25 (48) (2013) 485005.
[50] X. Huang, et al., Oxidation behavior of 316L austenitic stainless steel in high temperature air with long-term exposure, Mater. Res. Express 7 (6) (2020) 066517, https://doi.org/10.1088/2053-1591/ab96fa.
[51] J.H. Park, Formation mechanism of spinel-type inclusions in high-alloyed stainless steel melts, Metall. Mater. Trans. B 38 (2007) 657–663.